AIAA 2002-0120

Application of a Non-Linear Frequency Domain Solver to the Euler and Navier-Stokes Equations

Matthew McMullen, Antony Jameson
and Juan J. Alonso
Stanford University, Stanford, CA 94305

40th AIAA Aerospace Sciences Meeting & Exhibit
January 14–17, 2002/Reno, NV

AIAA 2002-0120

Application of a Non-Linear Frequency Domain Solver to the Euler and Navier-Stokes Equations

Matthew McMullen,* Antony Jameson†
and Juan J. Alonso‡
Stanford University, Stanford, CA 94305

This paper presents a technique used to accelerate the convergence of unsteady flows to a periodic steady state. The basis of this procedure is to assume the time period of the solution's oscillation and to transform both the solution and residual using a discrete Fourier transform. However, this paper also presents a method which iteratively solves for the time period during the process of calculating a solution. These methods are amenable to parallel processing and convergence acceleration techniques such as multigrid and implicit residual averaging. The accuracy and efficiency of the technique is verified by Euler and Navier-Stokes calculations for a pitching airfoil whose period of oscillation is forced. The capability to identify the natural frequency of oscillation is verified by Navier-Stokes calculations for laminar vortex shedding behind a cylinder where the time period of oscillation is unknown a priori. Results show that a limited number of modes can accurately capture the major flow physics of these model cases.

Introduction

Unsteady flows still present a severe challenge to Computational Fluid Dynamics (CFD). In general these flows can be subdivided into two general classes. The first are unsteady flows where the boundary conditions are forcing the unsteadiness at predetermined frequencies. Examples of this include the internal flows of turbomachinery, the external flow fields of helicopter blades or propellers, and certain aero-elastic computations. The second general class of unsteady flows are where instabilities in the fluid mechanical equations induces unsteadiness in the flow field. Examples in this class include (but are obviously not limited to) vortex shedding behind a cylinder, and other fluid dynamic cases involving separated flows and free shear layers. Without experimental or simplified analytic models, the temporal frequencies are difficult to determine a priori for this second class. This paper will present a reduced order scheme capable of solving unsteady flows for both classes of problem. The motivation for developing this scheme is the need to reduce the cost of unsteady CFD simulations for complex flows.

In general, time accurate solvers are designed to capture any arbitrary time history in the evolution of the solution. There are many applications, however, such as helicopter rotors or turbomachinery where users are typically only concerned with the data once the solution has reached a periodic steady state. Nevertheless, the majority of the computational effort is expended in resolving the decay of the initial transients. Algorithmic efficiency is a function of the time duration associated with this decay rate and the time step permitted by the algorithm. This time step can be selected either as a function of the CFL condition required for stability, or as a function of the temporal accuracy required by the user. In turbomachinery cases, any time accurate algorithm will pay a substantial computational penalty. The decay rate of the initial transients is slowed by the physical propagation of waves through the length of the turbomachinery component. Each wave can reflect in the opposite direction as it contacts a new stage, or it can propagate through the blade passage. As waves propagate back and forth through the machine, the length scales of the system are dramatically increased, and the physical decay rate is substantially slowed. This situation is exacerbated in complex geometries where 100 time steps are often needed to resolve a fundamental period of the blade passing frequency.

A less expensive approach to the calculation of unsteady flows is to linearize the flow field about a mean flow solution and solve for the unsteadiness using a frequency domain approach.[1] Assuming that the disturbances are small compared to the mean flow values, the unsteady component of the solution can be expanded in a Fourier series and a decoupled equation is obtained for each of the fundamental modes in the expansion. This equation can be solved with small modifications

*Graduate Student, Student Member AIAA
†T.V. Jones Professor of Engineering, AIAA Fellow
‡Assistant Professor, AIAA Member

to typical steady-state solvers. The computational cost is proportional to the cost of the steady-state solution multiplied by the number of distinct modes required to attain a desired level of temporal accuracy. However the error in the linearization procedure becomes significant when the amplitude of unsteadiness in the flow is substantial, as happens in most real viscous flow examples.

Hall et al,[2,3] have proposed a harmonic balance technique for the fully non-linear Navier-Stokes equations. McMullen et al[4] have proposed an alternative technique in which the equations are solved in the frequency domain. For time-periodic flows, either method can be computationally more efficient than time-accurate approaches without requiring the assumptions of a linearized solution. In comparison with time accurate solvers, which are developed for arbitrary time histories, frequency domain methods assume the flow solution is periodic in time. This permits a substantial reduction in computational cost when compared with time accurate methods. As with the linearized method the cost is proportional to the cost of the steady-state solution multiplied by the number of temporal modes required. In contrast with the linearized methods, nonlinear frequency domain methods do not make assumptions which limit the magnitude of the unsteadiness in the flow field. This allows these methods to predict flow field behavior for a broader class of problems and provides solutions in which all the temporal modes are coupled together.

Until now, one of the major deficiencies in frequency domain solvers was the requirement that the user specify a priori the time period of the solution's oscillation. This paper will present a method to address this problem. Application of this method requires the user to provide an initial guess of the time period. The method then iteratively solves for the solution as the residual of the unsteady equations is minimized.

The Non-Linear Frequency Domain method calculates only a limited number of temporal modes in the solution. Because of this, this scheme is generally classified as a reduced order method.[5] These schemes typically trade a reduced level of computational accuracy for improvements in computational efficiency. Since each flow field presents different challenges the validity of the method must be verified on a case by case basis. In addition, this verification process should categorize the type of results which can be accurately predicted for each different flow field. Capturing only the dominant modes in the solution field can provide accurate estimates for global properties such as coefficient of lift and drag but may produce inferior results for individual unsteady pressure coefficients. In this paper we examine results from several different test cases and compare them to experimental data.

Governing Equations

Viscous unsteady fluid flows in two dimensions can be described by the Navier Stokes equations in integral form

$$\int_\Omega \frac{\partial W}{\partial t} dV + \oint_{\partial\Omega} \vec{F} \cdot \vec{N} ds = 0, \tag{1}$$

where

$$\begin{aligned} W &= \begin{bmatrix} \rho \\ \rho u \\ \rho v \\ \rho E \end{bmatrix} \\ \vec{F}_1 = f &= \begin{bmatrix} \rho u \\ \rho u^2 + p - \sigma_{xx} \\ \rho uv - \sigma_{xy} \\ \rho uH - u\sigma_{xx} - v\sigma_{xy} + q_x \end{bmatrix} \\ \vec{F}_2 = g &= \begin{bmatrix} \rho v \\ \rho uv - \sigma_{xy} \\ \rho v^2 + p - \sigma_{yy} \\ \rho vH - u\sigma_{xy} - v\sigma_{yy} + q_y \end{bmatrix}, \end{aligned} \tag{2}$$

and $\vec{N}$ is the outward pointing normal on the surface of the control volume. The variables ρ, u, v, and E are density, Cartesian velocity components and specific total energy respectively. The flux terms also contain the thermodynamic pressure, p, the stress tensor, σ, and the heat flux vector obtained from Fourier's heat conduction law, $\vec{q}$. Closure is provided by the following equations for the pressure, shear stresses, and heat conduction.

$$\begin{aligned} p &= (\gamma - 1)\rho \left[e - \frac{1}{2}(u^2 + v^2) \right] \\ \sigma_{xx} &= 2\mu u_x - \frac{2}{3}\mu(u_x + v_y) \\ \sigma_{yy} &= 2\mu v_y - \frac{2}{3}\mu(u_x + v_y) \\ \sigma_{xy} &= \sigma_{yx} = \mu(u_y + v_x) \\ q_x &= \kappa \frac{\partial T}{\partial x} = -\frac{\gamma}{\gamma - 1}\frac{\mu}{Pr}\frac{\partial \frac{p}{\rho}}{\partial x} \\ q_y &= \kappa \frac{\partial T}{\partial y} = -\frac{\gamma}{\gamma - 1}\frac{\mu}{Pr}\frac{\partial \frac{p}{\rho}}{\partial y}. \end{aligned} \tag{3}$$

The equations can be discretized by dividing the flow domain into smaller cells. The volume of each cell is denoted by V. Applying Eq. 1 to each cell in the mesh, we can take the time derivative operator outside of the integral sign and the remaining integral can be approximated by the product of the cell volume and the current value of the flow solution at the cell center. The boundary integral is calculated by discrete integration of the fluxes around the control volume in a manner which is equivalent to central differencing. A modified JST scheme[6,7] is implemented to add third-order artificial dissipation for numerical stability. Thus Eq. 1 may be expressed as

$$V \frac{\partial W}{\partial t} + R(W) = 0. \tag{4}$$

Here

$$R(W) = \sum_{j=1}^{n} \vec{F}_j \cdot \vec{S}_j \tag{5}$$

is he residual for each cell, and $vecF_j$ is the flux through the cell face with area $\vec{S}_j$.

Under the assumption that the solution is periodic over a given time period, we can transform the independent variables and residual terms into the frequency domain using a discrete Fourier transform. In the following discussion, the variables $\hat{W}_k$ and $\hat{R}_k$ represent the Fourier coefficients (for a given wavenumber k) of the Fourier transforms of W and $R(W)$ respectively. Numerically this transformation is accomplished using the Fast Fourier Transform (FFT) in order to minimize the cost of computation. The computational cost of this transform is proportional to $N \log N$, where N is the number of time intervals used to describe the signal. For real solutions the Fourier coefficients for the negative wavenumbers are simply the complex conjugates of the coefficients for the positive wavenumbers. By taking advantage of this property we can eliminate half of the wavenumbers from the computation. Once we have obtained the Fourier coefficients for the expansions of W and $R(W)$, we can recover these quantities using the inverse discrete Fourier transform as follows:

$$\begin{aligned} W &= \sum_{k=-\frac{N}{2}}^{\frac{N}{2}-1} \hat{W}_k e^{ikt} \\ R(W) &= \sum_{k=-\frac{N}{2}}^{\frac{N}{2}-1} \hat{R}_k e^{ikt}, \end{aligned} \tag{6}$$

where

$$i = \sqrt{-1}.$$

If we apply the discrete Fourier transform to the semi-discrete form of the governing equation in Eq. 4, and we move the time derivative of the state variable inside the series summation, orthogonality of the Fourier series ensures that the individual contributions from each wavenumber are separately equal to zero

$$ikV\hat{W}_k + \hat{R}_k = 0. \tag{7}$$

It follows that a periodic steady-state equation can be written for each independent wavenumber.

Instead of directly solving Eqs. 7 we add in a pseudo-time derivative and numerically integrate the resulting equations

$$V\frac{d\hat{W}_k}{d\tau} + ikV\hat{W}_k + \hat{R}_k = 0 \tag{8}$$

to reach a steady state solution satisfying Eq. 7. Note, however, that solution of the physical problem will require iteration between physical and Fourier spaces, since, due to the nonlinearity of the residual operator, $R(W)$, $\hat{R}_k$ cannot be computed directly from $\hat{W}_k$. $\hat{R}_k$ can only be computed by evaluation of the residual at a number of time locations within one periodic cycle and subsequent transformation to Fourier space using the discrete Fourier transform.

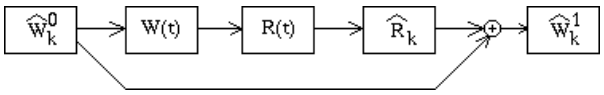

Fig. 1 Process Flowchart

Figure 1 provides a flow chart of the data and transforms used to advance the solution through one iteration in pseudo time. At the beginning of this iteration we know $\hat{W}$ at every grid point for all wavenumbers. This initial guess can simply result from the discrete Fourier transform of a constant uniform flow. Using an inverse FFT we can transform $\hat{W}$ back to the state vector $W(t)$ in time at every grid point. At each time point we compute the residual R, and, using an FFT we transform it back to the frequency domain to obtain $\hat{R}$. We calculate the overall residual by adding $\hat{R}$ to the source term $ikV\hat{W}$. This overall residual, specified in the frequency domain, is used to compute the new approximate $\hat{W}$, and the process returns to the beginning of the cycle.

Solution Techniques

The modified Eq. 8 represents the solution of a steady system of equations in the frequency domain. This facilitates established convergence acceleration (originally developed for steady systems) techniques to improve computational efficiency. A V or W cycle full multigrid scheme with variable local pseudo-time steps and implicit residual averaging has been implemented. The solution at each grid point is advanced in pseudo time using a modified multi-step RK scheme. Except for the residual averaging operations, the explicit nature of the time advancement scheme facilitates parallelization. The current solver utilizes multiple blocks distributed on different processors. A dual halo scheme serves to locally retrieve the state vector from neighboring grids. MPI libraries implement the actual communication between processors. The amount of inter-block communication scales linearly with the number of wavenumbers the user specifies a priori.

Gradient Based Methods for Determining the Time Period

For the class of flows where the time period of oscillation is not known a priori we propose a method to iteratively determine this parameter. This method is based on forming a gradient of the residual with respect to the time period. This gradient information is then used to iteratively update the time period

as convergence is obtained for the unsteady flow solution. Thomas et al[8] have proposed a harmonic balance method that solves the unsteady equations in the time domain. They argue that working in the time domain is easier, and facilitates reuse of existing codes. However, solving the equations in the frequency domain provide obvious approaches to forming gradients that are the basis of this method.

To begin the derivation, the wavenumber k is calculated by normalizing the sinusoidal period of oscillation 2π by the time period of interest T.

$$k = \frac{2\pi n}{T} \tag{9}$$

The unsteady residual in Eq. 8 can be can then be written as a function of the time period T.

$$-V\frac{d\hat{W}_n}{d\tau} = \frac{i2\pi nV}{T}\hat{W}_n + \hat{R}_n \tag{10}$$

The process of finding a solution to the unsteady flow equations is analogous to an optimization problem where the magnitude of the unsteady residual is minimized. We can calculate a gradient of this unsteady residual with respect to the time period. This gradient may then be used to iteratively modify the time period until the unsteady residual is minimized.

In order to implement this concept, we rewrite our unsteady residual as a figure of merit $\hat{I_n}$ defined for each wavenumber.

$$\hat{I_n} = -V\frac{d\hat{W}_n}{d\tau} \tag{11}$$

Because $\hat{I_n}$ is a complex quantity we minimize the square of the magnitude of this quantity. We can form a gradient of this cost function with respect to the time period as

$$\frac{1}{2}\frac{\partial\left|\hat{I_n}\right|^2}{\partial T} = \hat{I}_{nr}\frac{\partial\hat{I}_{nr}}{\partial T} + \hat{I}_{ni}\frac{\partial\hat{I}_{ni}}{\partial T} \tag{12}$$

The quantity $\hat{I_n}$ is already calculated while monitoring the convergence of the solution (note that the real and imaginary parts of $\hat{I_n}$ are $\hat{I}_{nr}$ and $\hat{I}_{ni}$ respectively). The partial derivative terms can be expanded in the following equations.

$$\frac{\partial\hat{I}_{nr}}{\partial T} = \frac{2\pi nV\hat{W}_{ni}}{T^2} \tag{13}$$

$$\frac{\partial\hat{I}_{ni}}{\partial T} = -\frac{2\pi nV\hat{W}_{nr}}{T^2} \tag{14}$$

The formulas can be further simplified by introducing cross product notation. We can write the fourier coefficient of the solution and residual in terms of two vectors.

$$\begin{aligned}\vec{W_n} &= \hat{W}_{nr}\hat{i} + \hat{W}_{ni}\hat{j} \\ \vec{I_n} &= \hat{I}_{nr}\hat{i} + \hat{I}_{ni}\hat{j}\end{aligned} \tag{15}$$

Description	Variable	Value
AGARD Case Number		CT6 DI 55
Airfoil		64A010
Mean Angle of Attack	α_m	0.00
Angle of Attack Variation	α_0	$\pm 1.01^\circ$
Reynolds Number	Re_∞	$12.56x10^6$
Mach Number	M_∞	0.796
Reduced Frequency	k_c	0.202

Table 1 AGARD Test Case Descriptions

Using this notation the gradient can be expressed as the magnitude of the cross product of the above vectors.

$$\frac{1}{2}\frac{\partial\left|\hat{\vec{I}_n}\right|^2}{\partial T} = \frac{2\pi nV}{T^2}|\vec{I_n}\times\vec{W_n}| \tag{16}$$

The time period can be updated using the gradient information by selecting a stable step ΔT.

$$T^{n+1} = T^n - \Delta T\frac{\partial\left|\hat{I_n}\right|^2}{\partial T} \tag{17}$$

Typically one can start with an initial guess in the vicinity of the final answer for the time period. An unsteady flow solution can be obtained by solving the unsteady equations to some residual level. The above gradient can then be used to adjust the time step at each iteration in the solution. The solution and gradients are hence simultaneously updated, and a final solution can be calculated to any arbitrary residual level.

Results - Pitching Airfoil

In the following subsections we present results from numerical simulations of the Euler and Navier-Stokes equations for a two dimensional airfoil undergoing a periodic pitching motion. The motion of the airfoil is identical to the experiments performed by Davis.[9] The characteristics of the test are summarized in Table 1.

Euler Equations

Two separate grid configurations were used to generate the Euler results. The first grid configuration was an "O-mesh" generated by a conformal mapping procedure. The second topology was a "C-mesh" which was generated using a hyperbolic grid generation tool. Table 2 provides a list of the different grids used in the Euler studies. Figures 2 and 3 depict the near field resolution of both the "O-mesh" and "C-Mesh" grids respectively.

It should be noted that the measured coordinates of the experimental cross-section do not exactly match the 64A010 theoretical profile. The deviation between

Topology	Dimensions	Mean Boundary Distance (Chords)	Mean Grid Spacing at Wall (Chords)
O-mesh	81x33	128	0.0096
O-mesh	161x33	128	0.0097
C-mesh	129x33	22	0.0087
C-mesh	193x49	22	0.0087

Table 2 Euler Mesh Descriptions

theoretical[12,13] and measured coordinates is plotted in Figure 5. The impact this deviation had on the solution was investigated using the higher fidelity Navier-Stokes solutions presented in upcoming sections. For the Euler simulations, the theoretical coordinates for the 64A010 airfoil were used in all cases.

In general, the Euler solutions were relatively insensitive to mesh variations. Steady state simulations were run and compared to the subsonic experimental results of Peterson.[14] The results of all the numerical simulations reproduce the experimental results with sufficient accuracy; verifying the spatial resolution of all the grids.

On each mesh listed in Table 2 we have computed solutions which use 1,2 and 3 temporal modes for a total of 12 different solutions. Coefficient of lift (C_l) data as a function of angle of attack, for all solution permutations, is provided in Figure 6. It is noteworthy, that little deviation in the global coefficients is achieved with additional temporal resolution. One can conclude that Euler solutions can be obtained with only one mode; which incurs the lowest possible computational cost. The magnitude of the C_l ellipse is larger than the experimental results for every case. Having verified the spatial accuracy of the grid, and investigated the effect of increasing temporal resolution; it seems that the over prediction of the C_l experimental results may be attributed to the lack of viscous damping in the governing equations, or to errors in the experimental data. Comparisons with the viscous results in the following sections tend to support this assertion.

Figure 7 provides coefficient of moment (C_m) data for the "C-mesh" cases listed in Table 2. The C_m data deviates badly from the experimental results. The trend is not surprising, considering that previous investigators, using similar spatial discretizations,[10] showed similar discrepancies between the data and time accurate computations of this flow field.

Navier Stokes Equations

A "C-mesh" grid configuration was used exclusively to generate the Navier-Stokes results. The grids were generated with the same hyperbolic mesh generation tool used in the previous section. Parameters defining the three different grids used in this survey are provided in Table 3. The highest density grid, 257x65 points, is displayed in Figure 4.

Topology	Dimensions	Boundary Distance (Chords)	Mean Grid Spacing at Wall (y+)
C-mesh	129x33	15	11.6
C-mesh	193x49	12	6.9
C-mesh	257x65	12	3.8

Table 3 Viscous Mesh Descriptions

Each set of parameters defined in Table 3 were used to generate grids around both the 64A010 airfoil and the measured airfoil of the CT6 experiment. All of these grids were used to provide solutions employing 1,2 and 3 temporal modes. Nine different solutions were created for grids based on the 64A010 coordinates, and another nine solutions were created for the measured coordinates of the experimental CT6 airfoil.

For the 64A010 coordinates, the coefficient of lift results are provided in Figure 8. The variation in C_l is minimal throughout the range of grid and mode combinations. The coarsest mesh using only a single mode provides a reasonable approximation to the higher resolution cases. Although the viscous terms have mitigated the effect, there is still a tendency for the numerical data to overshoot the experimental results.

Coefficient of lift results for the CT6 experimental airfoil are provided in Figure 9. Since the measured coordinates are not perfectly symmetric, there is a slight amount of asymmetry in the ellipses. Comparison of Figures 8 and 9 shows that there is a significant amount of variation in the C_l data for a slight variation in the airfoil geometry.

The coefficient of moment data is more sensitive to variations in the solution than the C_l data. Figures 10-12 provide C_m data as function of angle of attack for each mesh used in this survey. The coarsest mesh provides small variations in C_m over the range of temporal modes employed in the solution. The finer meshes, capable of resolving a larger number of temporal modes, show some variation in C_m with temporal accuracy. In both cases, the magnitude of the ellipse (formed by the numerical results) is lessened with an increasing number of modes. This effect slightly moves the numerical results closer to the experiment data, but the difference between the two sets is still significant.

Due to the variation in the numerical results, C_m data for both the CT6 experimental airfoil and 64A010 airfoil are provided in Figure 13. The differences noted above (between the CT6 and 64A010 solutions) in the C_l data are further magnified by the sensitivity of the C_m data. The figure shows that there is a significant variation in the moment coefficient over the entire range of solution permutations.

Mesh	1 Mode (secs/cycle)	2 Modes (secs/cycle)	3 Modes (secs/cycle)
129x33	0.59	1.0	1.5
193x49	1.9	2.9	4.5

Table 4 Execution Time

Computational Cost

This subsection provides data on the computational cost of the nonlinear frequency domain solver. We will provide data on the convergence rates of the force coefficients and the execution speed of the code. For the C_l and C_m convergence surveys, we will narrow our focus to solutions using only one temporal mode. In addition, we will only provide data for two different grid configurations. The 129x33 "C-mesh" will be used for all the Euler results and the 193x49 "C-mesh" will be used in the compilation of the viscous results.

Figures 14- 15 provide coefficient of lift data (for both Euler and Navier-Stokes cases) as a function of the number of multigrid cycles used in the solver. The Euler solver provides a converged C_l solution within 10 to 15 cycles. Due to the increased condition number, the convergence rate of the Navier-Stokes solver is slower. This latter case takes approximately 60 cycles to provide a reasonably converged result. Figures 16-17 provide coefficient of moment data as a function of the number of multigrid cycles. A trend similar to the C_l data is observed, with 20 to 30 cycles required to converge the Euler case, and 120 cycles for the viscous case.

The speed at which the code executes is provided in Table 4. The matrix provides execution times (in terms of seconds per multigrid cycle) as a function of the number of temporal modes used in the solution. The results were collected using a desktop computer equipped with an AMD 1.4Ghz Athlon processor. Note that the number of cycles required to converge the global coefficients is roughly independent of the number of temporal modes used in the solution. The required execution time can be approximated by the product of the number of required multigrid cycles and the amount of time needed per cycle. All the timing runs use 64 bit floating point arithmetic. 32 bit math can be utilized and will reduce execution times by approximately 50 percent. The timing results confirm that the computational cost approximately grows like $2N+1$, where N is the number of unsteady modes (not including the time average) used in the solution.

Results - Cylinder Flow

Our second test case is the laminar flow around a circular cylinder. At Reynolds numbers between 49 and 194[15] vortices alternately shed off behind the cylinder into a two-dimensional wake known as a Karman vortex street. The unsteady perturbations in this wake are substantial and represent a good test of the nonlinear frequency domain method. In contrast with the forced oscillations of the pitching airfoil, the vortex shedding is a function of instabilities in the shear layer of the flow, and the shedding frequency is not known a priori. Experimental methods or simplified analytic techniques can be used to provide initial guesses at this parameter. But the exact shedding frequency predicted by the discretized equations is unknown at the start of any numerical investigation.

Last year, McMullen et al[4] presented results for this cylinder flow case at Reynolds number of 180. These results were produced without the ability of varying the time period. Instead, the Strouhal number was fixed a priori based on experimental results. Coefficient of drag and pressure results from this previous paper are included in Table 5. The experimental results cited by this paper are included in Table 6. Counter intuitively, the predicted base suction coefficient deviates away from the experimental data as temporal resolution is increased.

Temporal Modes	$-C_{pb}$	C_d
1	0.832	1.257
3	0.895	1.306
5	0.903	1.311
7	0.903	1.311

Table 5 Time Averaged Data versus Temporal Modes Source: McMullen et al[4]

Experiment	$-C_{pb}$	C_d
Williamson and Roshko[16]	0.8265	
Henderson[17]	0.83	1.34

Table 6 Time Averaged Experimental Data

Here we present a new set of results generated by the Gradient Based Variable Time Period (GBVTP) algorithm. These results are compiled from a sweep of simulations over a range of Reynolds numbers and temporal accuracies. This sweep encompassed 40 different numerical simulations. Ten different Reynolds numbers were simulated between 60 and 150. For each Reynolds number, 4 separate simulations were run with 1,3,5 and 7 time varying harmonics. This breadth of simulations will statistically give a better estimate in the accuracy of these solutions; eliminating any random results that can occur with a single point comparison.

The grid used in these simulations is identical to the grid previously employed by McMullen et al.[4] Figure 18 displays this grid directly near the cylinder wall. The dimensions are 256 by 128 points in the circumferential and radial directions respectively. The mesh boundary is 200 chords from the center of the cylinder. An exponential function stretches the grid in the radial direction with the smallest spacing of $3.54e-03$

chords occurring at the wall. At the top of the cylinder roughly 15 grid points capture the boundary layer.

Figures 19- 21 show the Strouhal frequency, mean base suction coefficient, and mean drag coefficient as functions of Reynolds number and temporal accuracy. For the purpose of validation, experimental results from Williamson et al[16,18–21] and numerical results from Henderson et al[17] are plotted on these figures. The latter numerical experiments are considered highly accurate. They employ a spectral element method based on 8^{th} order accurate polynomials.

Unlike our previous results, our new predictions converge toward the experimental results as temporal accuracy is increased. For the cases where more than one temporal mode was used, the percentage difference in the Strouhal data between the experiment and numerical results is approximately 3.5 percent. This error is consistent throughout the range of Reynolds numbers, with the numerical simulations constantly under predicting the experimental values. When a single harmonic is used, we observe another under predicting trend. In this case, the numerical Strouhal data becomes a better approximate of the experimental results as the Reynolds number decreases.

Unlike the Strouhal data, the mean base pressure coefficient converges to experimental values at the lower Reynolds number for all different temporal resolutions. As the Reynolds number increases, only the least accurate solution drastically diverges. Slightly different observations can be made for the mean drag coefficient data. At the higher temporal resolutions, the numeric results consistently under predict the mean drag coefficient data of Henderson. When the components of drag are separated into viscous and pressure components the same trend holds true.

The convergence patterns of the global coefficients suggest that the magnitude of the higher harmonics in the exact solution continues to increase with increasing Reynolds number. This observation is supported by Figure 22 which shows the L_2 norm of the magnitude of the solution's Fourier coefficient. As the Reynolds number decreases the decay rate in the solutions higher harmonic increases. For the lower temporal accuracy simulations, the error incurred by the unresolved frequencies in the solution decays as the Reynolds number decreases.

We now examine this equation: If one does not use a variable time period algorithm, how accurate is the solution based on any close guess of the Strouhal number? This question is partially answered in Figures 23 and 24 which quantify the minimum residual as a function of the distance between the exact Strouhal number and one used in fixed Strouhal number simulation. The data was generated by first obtaining the exact Strouhal value using a gradient based technique. Subsequent fixed Strouhal number simulations were run at Strouhal number perturbed a given distance from the exact value. Each simulation would converge to a residual level greater than the machine zero value. This is the residual plotted in semi-log format in Figure 23 and log-log format in Figure 24. With these figures one can estimate the convergence error in the solution as a function of Strouhal number; since the residual scales with the distance between an approximate solution and the exact one. This supports the assertion that there is a unique time period that provides an exact (machine level representation) solution to the discretized equations.

Conclusions

The numerical results confirm the accuracy and computational efficiency of the nonlinear frequency domain method which we have implemented for several challenging problems of significant practical importance.

For the cylinder shedding test case, relatively accurate global coefficients were obtained using three temporal modes. For the forced pitching airfoil case only one temporal mode was needed to accurately predict the coefficient of lift. Experimental data for the coefficient of moment is poorly predicted. The limited number of modes needed for each case confirms the promise that this method can provide a computationally efficient algorithm for complex problems.

We have also shown that in problems like vortex shedding from the cylinder, the dominant natural frequency can be predicted by the Gradient Based Variable Time Period (GBVTP) method.

Acknowledgments

This work was sponsored by the Department of Energy under contract number LLNL B341491 as part of the Accelerated Strategic Computing Initiative (ASCI) program. The authors would like to acknowledge the help extended by Charles Williamson and Sanford Davis for their personal communication of their experimental results.

References

[1]K.C. Hall and W.S. Clark. Linearized Euler Predictions of Unsteady Aerodynamic Loads in Cascades. *AIAA Journal*, 31(3):540–550, March 1993.

[2]K.C. Hall. Seminar on Harmonic Balance Techniques, January 2000. Presented to the Aerospace Computing Lab, Stanford University.

[3]K.C. Hall, J.P. Thomas, and W.S. Clark. Computation of Unsteady Nonlinear Flows in Cascades using a Harmonic Balance Technique. Technical report, 9th International Symposium on Unsteady Aerodynamics, Aeroacoustics and Aeroelasticity of Turbomachines, Lyon, France, September 2000.

[4]M. McMullen, A. Jameson, and J. Alonso. Acceleration of Convergence to a Periodic Steady State in Turbomachinery Flows. *AIAA paper 01-0152*, AIAA 39th Aerospace Sciences Meeting, Reno, NV, January 2001.

[5]P. Beran and W. Silva. Reduced-Order Modeling: New Approaches for Computational Physics. *AIAA paper 01-0853*, AIAA 39th Aerospace Sciences Meeting, Reno, NV, January 2001.

[6]A. Jameson. Analysis and Design of Numerical Schemes for Gas dynamics I Artificial Diffusion, Upwind Biasing, Limiters and their Efect on Accuracy and Multigrid Convergence. *International Journal of Computational Fluid Dynamics*, 4:171–218, 1995.

[7]R.C. Swanson and E. Turkel. On Central-Difference and Upwind Schemes. *Journal of Computational Physics*, 101:297–306, 1992.

[8]J.P. Thomas, E.H. Dowell, and K.C. Hall. Nonlinear Inviscid Aerodynamic Effects on Transonic Divergence, Flutter and Limit Cycle Oscillations. *AIAA paper 01-1209*, 42nd AIAA/ASME/ASCE/AHS/ASC Structures, Structural Dynamics, and Materials Conference & Exhibit, Seattle, WA, April 2001.

[9]S.S. Davis. NACA 64A010 (NASA Ames Model) Oscillatory Pitching. *AGARD Report 702*, AGARD, January 1982.

[10]N.A. Pierce and J.J. Alonso. Efficient Computation of Unsteady Viscous Flow by an Implicit Preconditioned Multigrid Method. *AIAA Journal*, 36:401–408, 1998.

[11]J. Hsu and A. Jameson. Personal communications on unsteady flow solvers, April 2001.

[12]Ira Abbott and Albert Von Doenhoff. *Theory of Wing Sections*. Dover Publications Inc, New York,, 1959.

[13]Michael Selig. UIUC Airfoil Coordinates Database. Technical report, University of Illinois, February 2000.

[14]Robert Peterson. The Boundary-Layer and Stalling Characteristics of the NACA 64A010 Airfoil Section. *NACA Technical Report 2235*, NACA, November 1950.

[15]C.H.K. Williamson. Vortex Dynamics in the Cylinder Wake. *Annual Review Fluid Mech.*, 28:477–539, 1996.

[16]C.H.K. Williamson. Defining a Universal and Continuous Strouhal-Reynolds Number Relationship for the Laminar Vortex Shedding of a Circular Cylinder. *Phys. Fluids*, 31:2742, 1988a.

[17]R.D. Henderson. Details of the Drag Curve Near the Onset of Vortex Shedding. *Physics of Fluids*, 1995.

[18]C.H.K. Williamson and A. Roshko. Measurements of Base Pressure in the Wake of a Cylinder at Low Reynolds Numbers. *Z. Flugwiss. Weltraumforsch*, 1990.

[19]C.H.K. Williamson and G.L. Brown. A Series in (1/sqrt(Re)) to Represent the Strouhal-Reynolds Number Relationship of the Cylinder Wake. *J. Fluids and Struc.*, 1998.

[20]C.H.K. Williamson. The Existence of Two Stages in the Transition to Three-Dimensionality of a Cylinder Wake. *Phys. Fluids*, 31:3165, 1988b.

[21]C.H.K Williamson. Three-Dimensional Wake Transition. *J. Fluid Mech.*, 328:345–407, 1996.

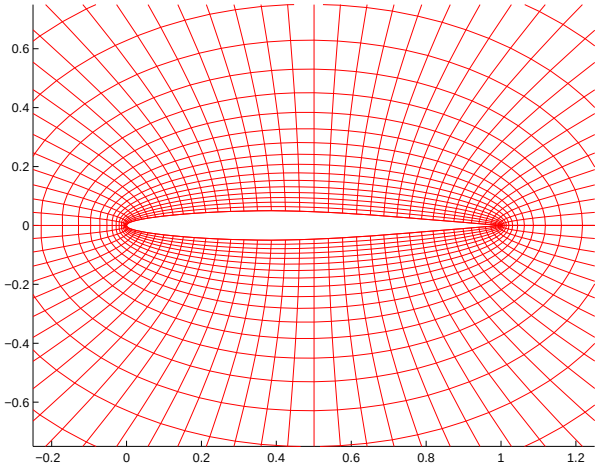

Fig. 2 Nearfield of 81x33 Euler "O-mesh"

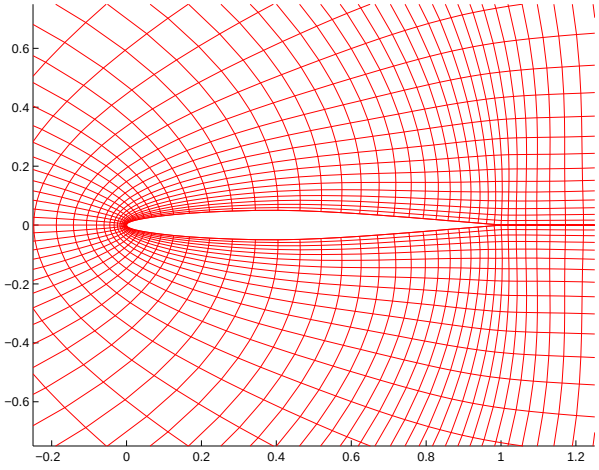

Fig. 3 Nearfield of 129x33 Euler "C-mesh"

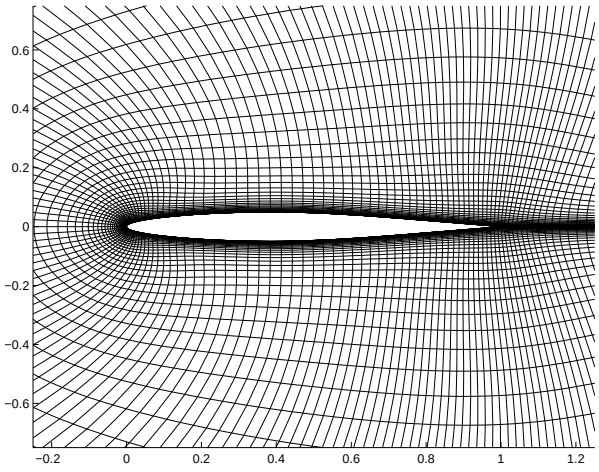

Fig. 4 Nearfield of 257x65 Viscous "C-mesh"

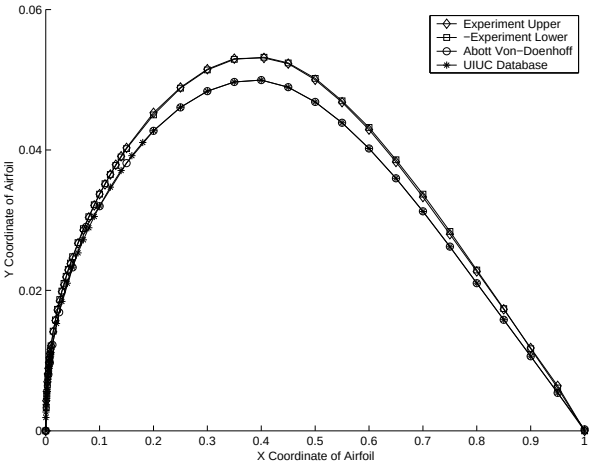

Fig. 5 Deviation Between Measured Coordinates of Experimental Foil and Theoretical 64A010 Airfoil

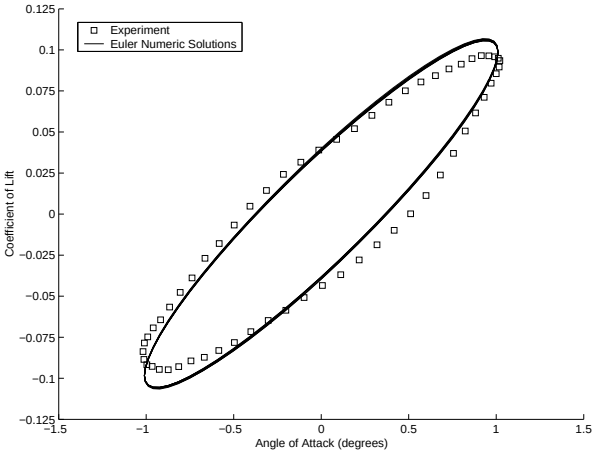

Fig. 6 Coefficient of Lift versus Angle of Attack - All Euler Solutions

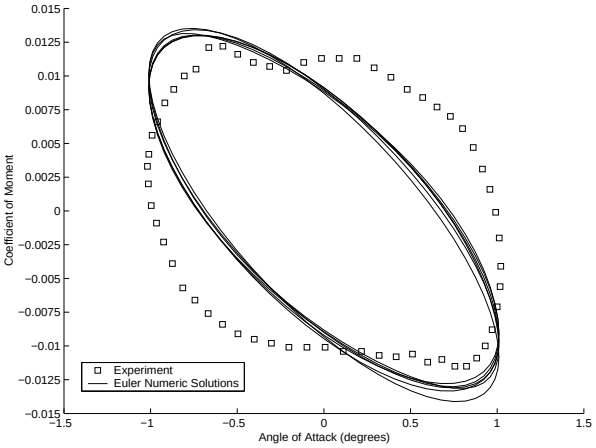

Fig. 7 Coefficient of Moment versus Angle of Attack - All Euler Solutions

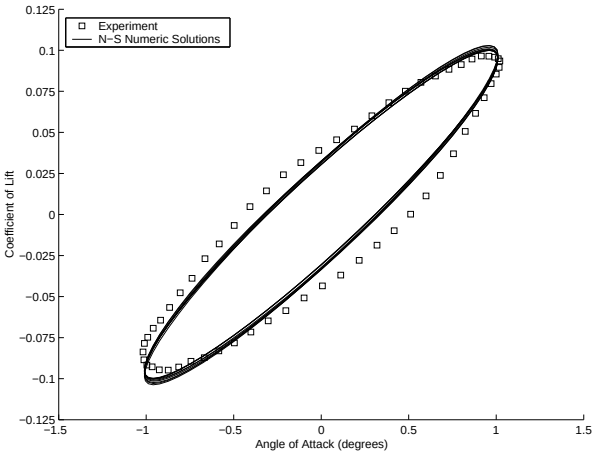

Fig. 8 Coefficient of Lift versus Angle of Attack - All Viscous Solutions of 64A010 Airfoil

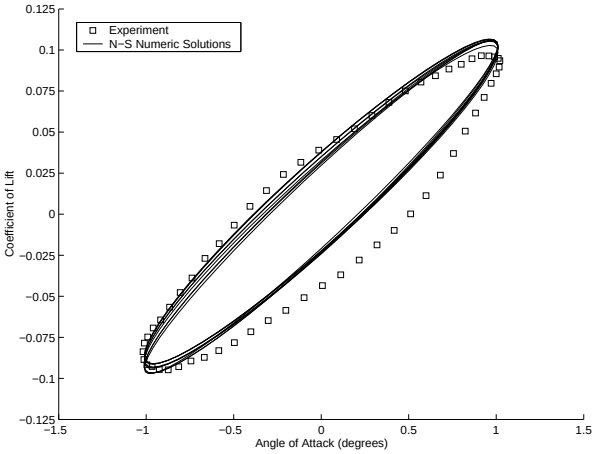

Fig. 9 Coefficient of Lift versus Angle of Attack - All Viscous Solutions of CT6 Experimental Airfoil

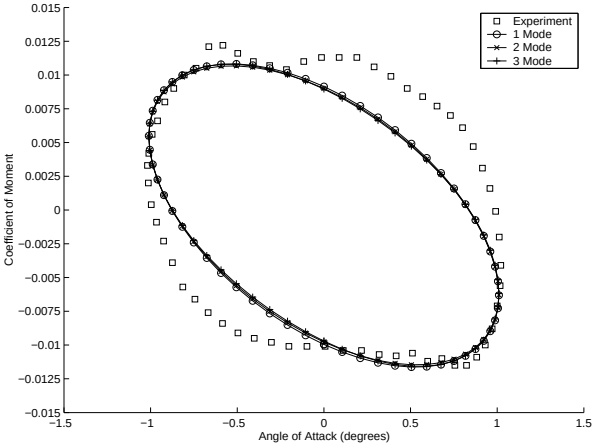

Fig. 10 Coefficient of Moment versus Angle of Attack - Viscous Solution - 129x33 Grid of 64A010 Airfoil

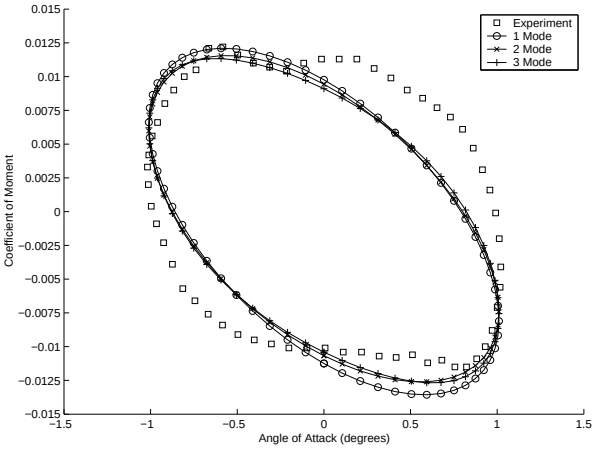

Fig. 11 Coefficient of Moment versus Angle of Attack - Viscous Solution - 193x49 Grid of 64A010 Airfoil

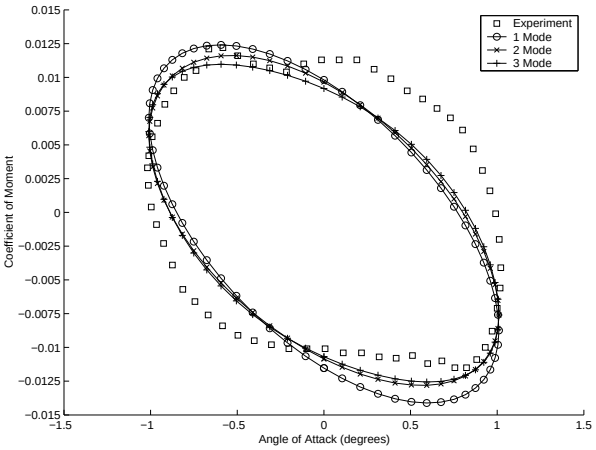

Fig. 12 Coefficient of Moment versus Angle of Attack - Viscous Solution - 257x65 Grid of 64A010 Airfoil

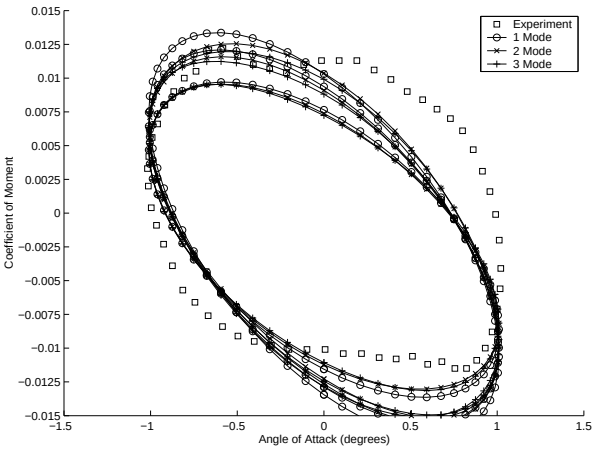

Fig. 13 Coefficient of Moment versus Angle of Attack - Viscous Solution - All Grids of CT6 Experimental Airfoil

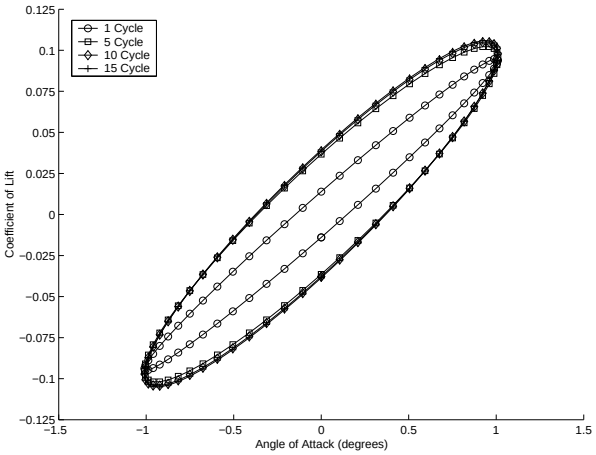

Fig. 14 Convergence of Coefficient of Lift versus Angle of Attack - Euler - 129x33 Grid

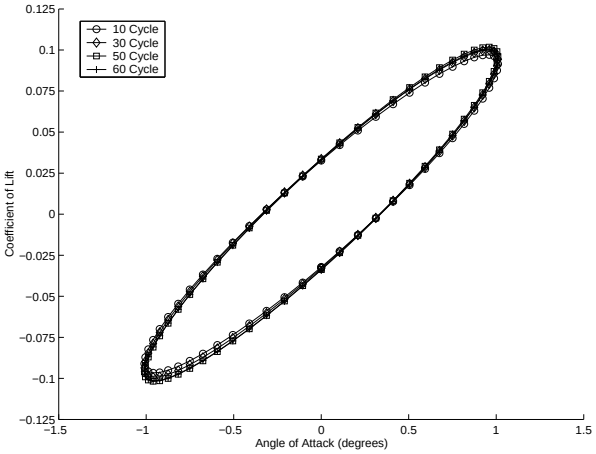

Fig. 15 Convergence of Coefficient of Lift versus Angle of Attack - Viscous - 193x49 Grid

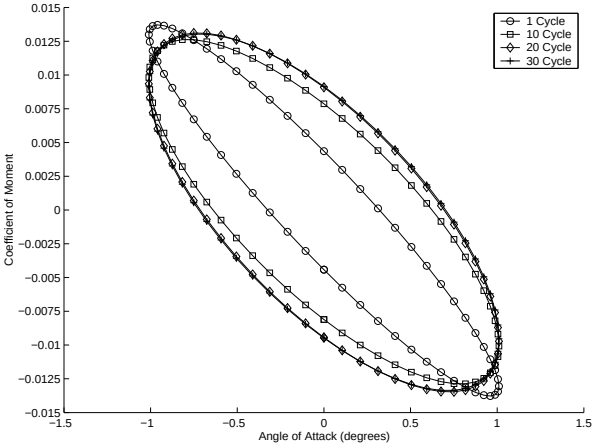

Fig. 16 Convergence of Coefficient of Moment versus Angle of Attack - Euler - 129x33 Grid

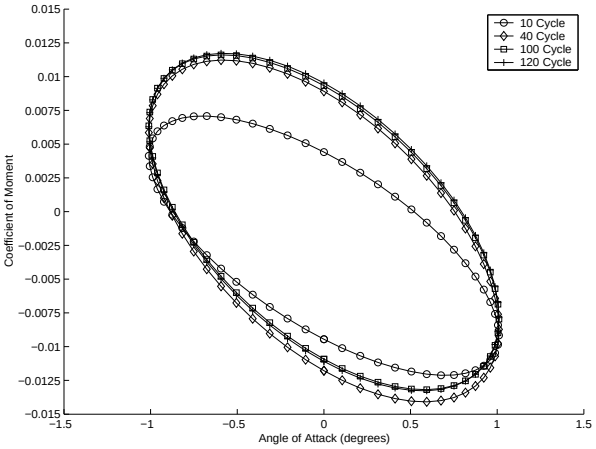

Fig. 17 Convergence of Coefficient of Moment versus Angle of Attack - Viscous - 193x49 Grid

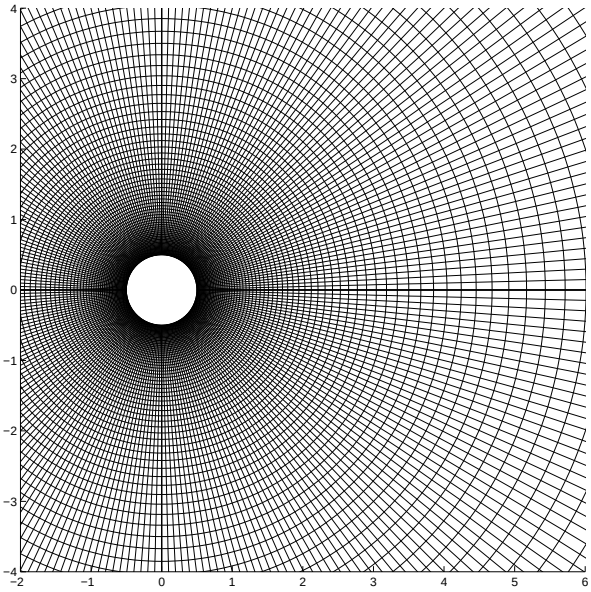

Fig. 18 Computational Grid for Cylinder Flow

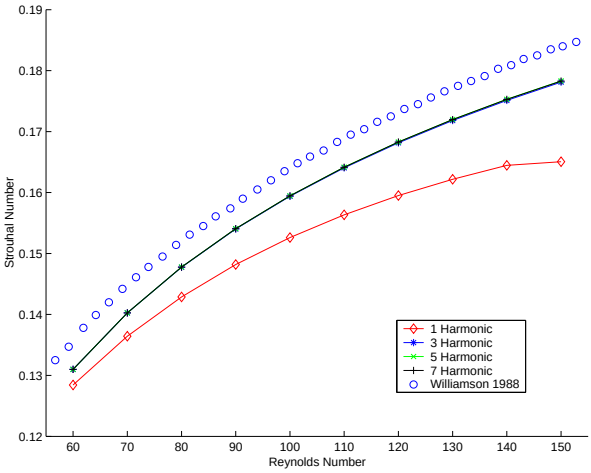

Fig. 19 Strouhal Numbers versus Reynolds Number For Laminar Vortex Shedding

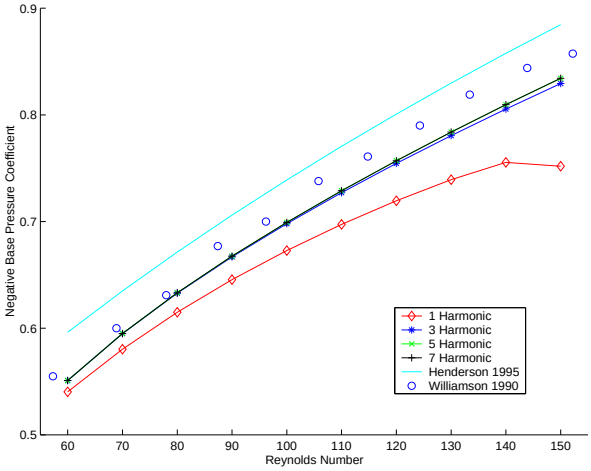

Fig. 20 Mean Base Pressure Coefficient versus Reynolds Number For Laminar Vortex Shedding

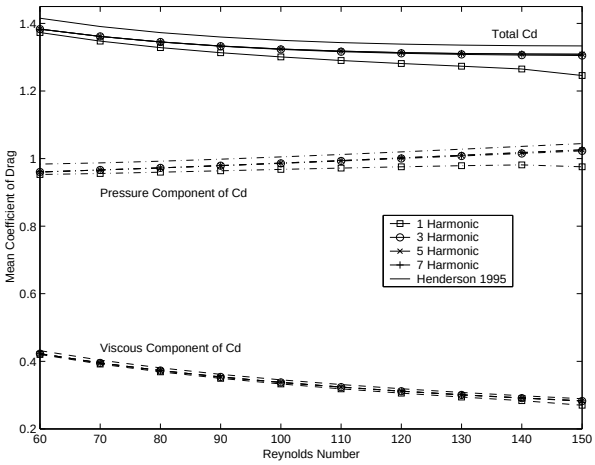

Fig. 21 Mean Coefficient of Drag versus Reynolds Number For Laminar Vortex Shedding

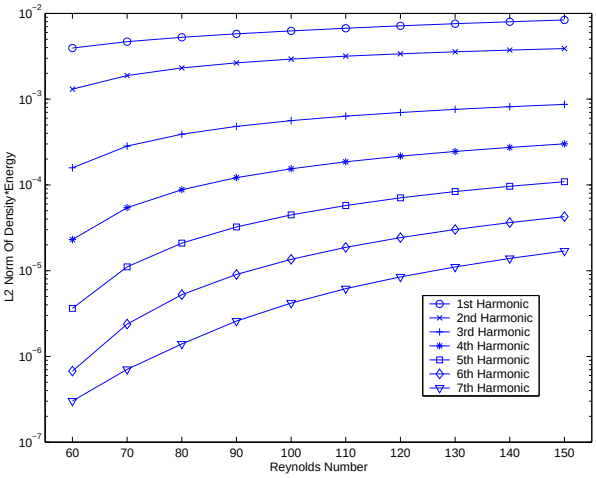

Fig. 22 L2 Norm of Solution Energy versus Reynolds For Laminar Vortex Shedding

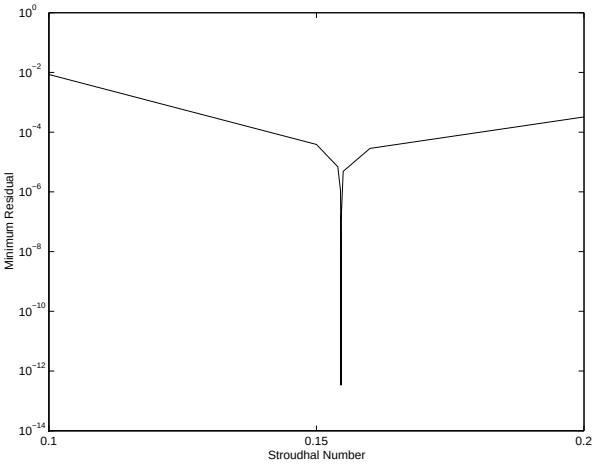

Fig. 23 Minimum Residual versus Strouhal Frequency

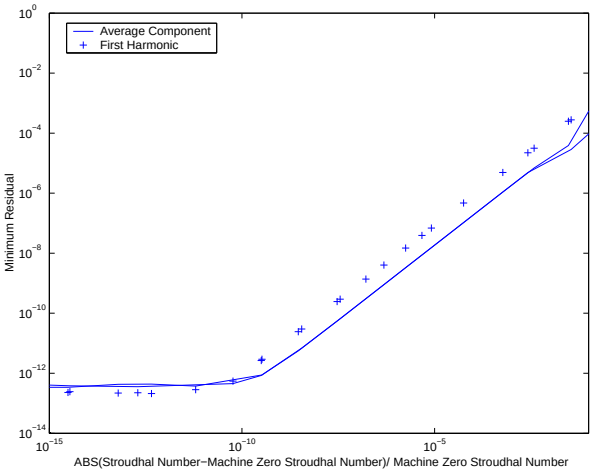

Fig. 24 Minimum Residual versus Strouhal Frequency